Three-Dimensional Orientation Sensors by Defocused Imaging of Gold Nanorods through an Ordinary Wide-Field Microscope

Tao Li,[†] Qiang Li,[†] Yi Xu,[†] Xiao-Jun Chen,[†] Qiao-Feng Dai,[†] Haiying Liu,[†] Sheng Lan,[†] Shaolong Tie,[‡] and Li-Jun Wu[†,*]
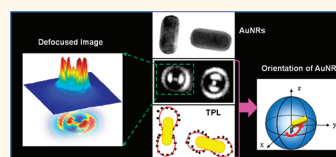
[†]Laboratory of Photonic Information Technology, School for Information and Optoelectronic Science and Engineering, and [‡]School of Chemistry and Environment, South China Normal University, Guangzhou 510006, People's Republic of China.

Optical probes for nanoscale orientation sensing have attracted much attention in the field of single-molecule spectroscopy.[1,2] In material research, local orientation sensors are frequently used to investigate, for example, liquid crystal orientation,[3] the dynamics of polymers near the glass transition temperature,[4] and the conformation and rotation of single polymer chains.[5,6] Likewise, the spatial orientation of the probes is of great significance in understanding certain vital biological mechanisms, such as the structural dynamics of myosin V,[7] the structure of Dendra-2-actin in fibroblast cells,[8] the rotational motions of nano-objects in live cells,[9] and the molecular dynamics of early virus—host couplings for cell infection.[10] Most of the currently employed probes are fluorescent labels, such as fluorescent polymers,[5] organic dyes,[7,9] and inorganic semiconductor nanoparticles.[10] However, time-dependent fluorescence fluctuations (photoblinking) and a limited lifetime due to irreversible photochemical changes (photobleaching) seriously restrict their use for imaging applications.[7,11,12] Although core—shell structured semiconductor nanoparticles could alleviate photobleaching to some degree,[13] the toxicity of these nanoparticles could be a fatal drawback for their practical applications in life science.[14]

Noble metal nanoparticles (NPs) exhibit extraordinary plasmonic properties, great photostability, excellent biocompatibility, and nontoxicity, making them an attractive alternative label to organic dyes or quantum dots.[15,16] In addition to generating magnitudes higher absorption and scattering cross sections than dye molecules,[17] the collective oscillation of their localized surface plasmons (LSPs) also gives rise to a strong polarization of the fluorescence, absorbed, and scattered light because of their inherent anisotropy.[2,18—20] This characteristic polarization response can be tuned by varying the shape of the NPs, which enables its use in orientation imaging.[21] One of the most interesting metallic NPs with an anisotropic shape is the Au nanorods (AuNRs), in which the longitudinal and transverse localized surface plasmon resonant (LSPR)

ABSTRACT Gold (Au) nanoparticles, particularly nanorods, are actively employed as imaging probes because of their special non-blinking and nonbleaching absorption, scattering, and emitting properties that arise from the excitation of surface plasmons. Herein, we report a novel sensing method that detects feature orientation at the nanoscale *via* the defocused imaging of individual Au nanorods (AuNRs) with an ordinary wide-field optical microscope. By simultaneously recording defocused images and two-photon luminescence intensities for a large number of individual AuNRs, we correlate their defocused images with their three-dimensional spatial orientations. The spatial orientation of many individual AuNRs can be monitored *in situ* and in real-time within a single frame, enabling its use as a technique for high-throughput sensing. The probe size can be as small as several nanometers, which is highly desirable for minimization of any potential interference from the probe itself. Furthermore, the sensing property is insensitive to the excitation polarization and the distribution of the probe aspect ratio, which allows AuNRs of any length within a proper regime to be used as orientation sensors without changing the laser frequency and polarization. These unique features make the orientation probes proposed here outstanding candidates for optical imaging and sensing in materials science and biological applications.

KEYWORDS: gold nanorods · two-photon luminescence · single-photon luminescence · orientation sensor · defocused imaging

modes are parallel and perpendicular to the rod length direction, respectively. For these reasons, Link *et al.* has proposed an orientation sensor based on the plasmonic absorbance of AuNRs.[1] However, it is difficult to extract the three-dimensional (3D) orientation information of AuNRs within a single frame with this kind of photothermal imaging technique. It also requires combining a time-modulated heating beam with a probe beam, which complicates the measuring process. Furthermore, the probe AuNR is easily melted and reshaped from excessive energy absorption.[22]

In the conventional imaging method, the 3D orientation of the specimen cannot be resolved within a single frame because the scattered or emitted light from all the dipoles on the focal plane is focused into a single Airy disk. If an aberration (slight shift of the dipole away from the focal plane) is deliberately introduced to the imaging system, the direct observation of the spatial distribution of the emitted or scattered field (defocused image) of single dipoles becomes possible. This technique is based on the electron transition dipole approximation and the fact that the dipole radiation exhibits angular anisotropy. Unlike conventional orientation imaging with two crossed polarizers, the defocused imaging method allows direct access to the 3D orientation of the emitters or scatterers as well as their radiation characteristics within a single frame.[23,24] Very recently, based on the strong scattering of surface plasmons (SPs), Yeung *et al.* resolved 3D orientations of single AuNRs by using a standard optical dark-field microscope and deciphering the defocused dark-field images.[25] Nonetheless, this scattering-based technique is complicated by the fact that many other biological objects can also scatter strongly and give rise to a large background, thereby decreasing the sensitivity. Additionally, the scattering cross-section scales with the radius (*r*) of the NP according to r^6.[17] Thus, metallic NPs much smaller than 50 nm in diameter are not detectable with this dark-field single-particle imaging technique,[17] inherently prohibiting its use in applications requiring smaller probe sizes.

If the radiation emitted by a single fluorophore can be approximated as a dipole, its emission characteristics can be conveniently investigated with defocused imaging.[26] Fluorescence from metal materials has been observed for more than thirty years but has not garnered much attention due to very low quantum yields of $\sim 10^{-10}$.[27] Recently, fluorescence with much higher quantum yield ($>10^{-5}$) has been observed in both metal nanoclusters (NCs) (<2 nm)[28] and small metal NPs (<100 nm).[29−31] The photoluminescence (PL) of Au NCs can be attributed to the radiative recombination of Fermi level electrons and sp- or d-band holes created after photoexcitation.[32,33] Although the size of the Au NC can be less than 2 nm, which is highly desirable for biosensing at the single-molecule level,
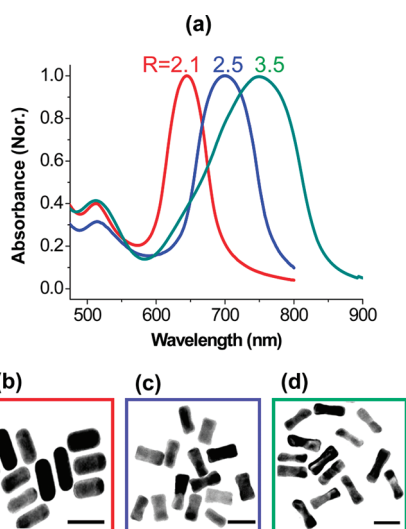
Figure 1. (a) Ensemble extinction spectra of AuNRs taken in aqueous solutions with average aspect ratios of 2.1 (red), 2.5 (blue), and 3.5 (green). (b−d) Corresponding representative TEM images of AuNRs. The scale bar dimension is 50 nm.

unfortunately, its fluorescence suffers from photoblinking and photobleaching.[34] When the size of the NP is large enough to support a "plasmon" characteristic of a large number of free electrons, its fluorescence is generally attributed to the radiative emission of the excited LSPR, where the excited d-band holes recombine nonradiatively with sp-electrons and emit particle plasmons.[30] When the aspect ratio of AuNR is less than 5, its excited plasmon mode becomes fundamental and exhibits dipolar character.[35] Thus its emission can be approximated as dipoles because of the collective oscillation of free electrons.

Two-photon luminescence (TPL) is expected to be a promising tool for optical sensing because two-photon processes respond quadratically with intensity, thus providing greatly enhanced sensitivity for investigation of individual AuNRs.[35] In fact, TPL is one of the most extensively studied processes related with the application of AuNRs.[36,37] Yet despite its heightened sensitivity, it cannot be applied in the defocused imaging technique because the excitation needs to be tightly focused. Fortunately, AuNRs can also be excited by a single-photon process with a proper wavelength,[29,38] which is employed in this work to generate defocused images that validate the use of AuNRs as new probes for 3D orientation sensing. By simultaneously recording defocused images and TPL intensities while tuning the incident polarization for a large number of individual AuNRs with aspect ratios of 1.2−4, we can correlate their defocused images with their 3D spatial orientations. This allows us to unambiguously derive the spatial orientation of multiple individual AuNRs and their radiation characteristics within a single frame. The technique we propose here is highly reliable and offers great advantages over

previously reported methods, which include a fast full 3D angle resolving capability, freedom from photobleaching and photoblinking, high throughput for probing, small probe size, and flexible excitation. These unique features make it an outstanding candidate for optical imaging and sensing in both materials science and biological applications.

RESULTS AND DISCUSSION

AuNRs were prepared chemically in aqueous solutions by a seed-mediated method.[39] Figure 1a illustrates the normalized UV–vis absorption spectra of the fabricated AuNRs with three typical aspect ratios. The transverse plasmon resonance band appears to be positioned at approximately 515 nm, while the maximum of the longitudinal plasmon resonance wavelength red shifts with increasing aspect ratio. Figure 1b–d show the corresponding transmission electron microscopy (TEM, JEM-2100HR) images. By analyzing these TEM results, the average aspect ratios of AuNRs were estimated to be 2.1, 2.5, and 3.5, respectively, which were confirmed by discrete dipole approximation (DDA) simulation through fitting the experimentally measured extinction spectra. The AuNRs were deposited on 0.2 mm thick cleaned glass coverslips at a low concentration (the coverage is less than one rod per μm^2). They are well-separated from each other.

The details for our experimental setup to investigate the defocused image and TPL polarization dependence of individual AuNRs are similar to what was shown in our previous papers[40,41] and schematically plotted in Figure S1. We normally choose the target AuNR by tracking its TPL intensity upon rotating the excitation (800 nm, 130 fs, 76 MHz) polarization at first. After that, we change the excitation wavelength to 532 nm (CW) and record the defocused images. The optical circuit has to be adjusted very carefully to ensure that we are probing the same AuNR during these two processes.

The program used to simulate defocused images is based on the multidimensional (3D here) dipole model developed by Enderlein et al.[26,42] The definition of the angular coordinates is shown in Figure S2, where Ψ is the out-of-plane angle (inclination angle between the rod length direction and optical axis), and β the in-plane angle.

It has been broadly accepted that the TPL intensity is maximized when the polarization of the excitation is parallel to the long axis of AuNRs[36,37] as the excitation of interband absorption and the longitudinal surface plasmon of AuNRs can result in enhanced local electric fields, which amplify both exciting and emission fields. It follows a $\cos^4 \theta$ dependence (θ is the angle between the excitation polarization and the long axis of the rod).[35] This polarization characteristic of the TPL
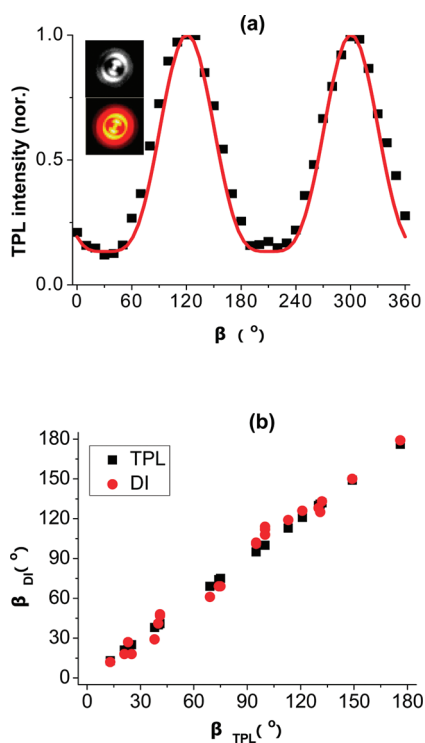
Figure 2. (a) Excitation polarization dependence of the TPL intensity integrated over 570−640 nm. The solid curve is fitted by a $\cos^4(\theta - 120.6°)$ function, and β is thus determined to be 120.6°. The inset shows the measured (white and black) and simulated (red and yellow) defocused images (DI). (b) AuNR orientations obtained from the excitation polarization characteristics of TPL (black square) and defocused images (red circle).

intensity can be applied to determining the orientation of the NR. Here we utilize this property to verify the orientation of the AuNRs derived from the defocused imaging technique. This process is not as complicated as fabricating an identification pattern on the glass substrates to position the individual AuNRs.[1,43] We start with a simple case in which the long axis of the AuNRs is nearly parallel to the cover slide.

Typical TPL spectra for two individual AuNRs with aspect ratios 2.0 and 3.5 are shown in Figure S3a. To avoid the influence from a second-harmonic generation of AuNRs, the TPL intensity was obtained by integrating over the wavelength range from 570 to 640 nm. Figure 2a plots its traces for a representative individual AuNR upon adjusting the excitation polarization, with the measured and simulated defocused images displayed in the inset. Unless specifically stated otherwise, the black and white defocused images correspond to the measured results, and colorful ones to simulated results. As seen, the intensity traces for TPL can be fitted to be a $\cos^4(\theta - \beta)$ function. The in-plane orientation of the AuNR can thus be deduced to be 113.6°. The corresponding defocused image shows a bilaterally symmetric two-lobe pattern. By fitting the experimental parameters into the simulation program, the angle β is derived to be 113°. The two closely
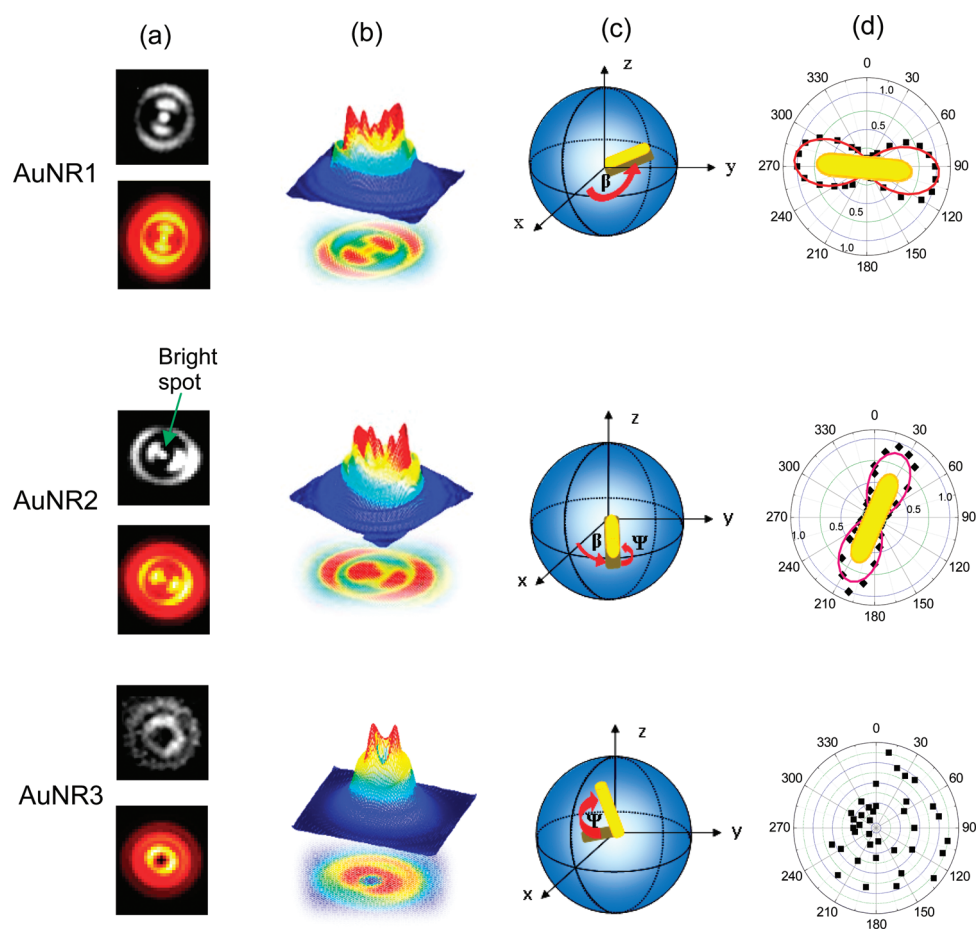
Figure 3. Column (a) demonstrates the measured (in white and black) and simulated (in red and yellow) defocused images for three typical AuNRs from a sample with an average aspect ratio of 3.5. The defocusing distance for AuNR1, AuNR2, and AuNR3 is 1, 1.1, and 0.92 μm, respectively. Column (b) plots the 3D intensity distribution of the measured defocused images in column (a). The 3D orientations of the single AuNRs determined from the defocused images are illustrated in column (c) as yellow rods, in which the gray rods are the corresponding in-plane projections. Column (d) shows the polar plots of the TPL intensity (black squares) *versus* the excitation polarization direction. The red curves are drawn according to the best-fitted $\cos^4(\theta-\beta)$ function. The orientations of the yellow rods are derived from the defocused images shown in column (a).

consistent results indicate that the defocused image of individual AuNRs can be applied as a novel orientation probe.

To back our conclusions with a statistically meaningful data set, we investigated the polarization characteristic of TPL for 30 individual AuNRs and simultaneously recorded their defocused images. Figure 2b illustrates the correlation of orientation angles for 30 AuNRs determined independently by these two techniques. The largest deviation is 14°. Several factors, such as the 10° step to rotate the excitation polarization, the difference between the optical circuits for single-photon (532 nm) and two-photon excitation (800 nm), and the process of fitting defocused images could introduce the deviation. However, the excellent correlation between the orientation angles obtained by the two techniques confirms that the spatial orientation of individual AuNRs can be unambiguously determined by the defocused imaging technique.

When the AuNR is orientated out of plane, *i.e.*, $0° < \Psi < 90°$, we can also decipher its spatial orientation

by fitting the defocused images. A map of simulated defocused images from individual AuNRs with some typical 3D orientations is shown in Figure S4. Obviously, each specific group of angles is correlated with a unique defocused image. Therefore, the random orientation of AuNRs could be easily determined by referring to their corresponding emitting field map. The resolving ability for in-plane and out-of-plane (between 30° and 90°) angles can reach 1 degree.[44] It is worth noting that, for the out-of-plane-orientated AuNRs, the two most obvious characteristics of the defocused images are the 2-fold symmetry breaking of the brightness of the high-order diffraction ring (when $90° > \Psi > 30°$) and the bright spot at the center deviating away from the central position (when $0° < \Psi < 30°$). As is known, the 2D in-plane orientation (the projection of the oscillation dipole onto the image plane) of AuNRs could be accurately determined *via* modulating the excitation polarization.[25] For the out-of-plane angle, we utilize a parameter DOP = $(I_{max} - I_{min})/(I_{max}+I_{min})$, where I_{max} and I_{min} are the maximum and minimum
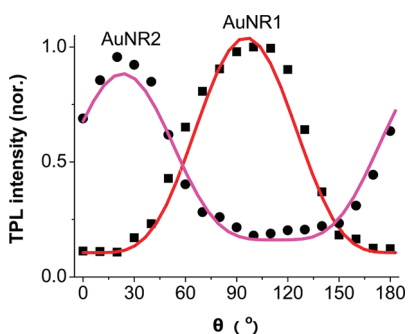
Figure 4. Excitation polarization dependence of the TPL intensity integrated over 570−640 nm for AuNR1 (squares) and AuNR2 (circles) demonstrated in Figure 3. The solid curves are fitted by $\cos^4(\theta-95.6°)$ (red) and $\cos^4(\theta-24.3°)$ (magenta) functions, respectively. Obviously, the DOP of AuNR1 is larger than that of AuNR2.

luminescence intensities at two perpendicular polarization directions, for qualitative analysis. When the AuNR is orientated out of plane, its DOP should be smaller than that for the in-plane-positioned AuNR. Column (a) in Figure 3 shows the measured and simulated defocused images of three typically selected AuNRs. Through fitting the field distribution pattern, the 3D angles of the AuNRs are measured to have out-of-plane angles of 0°, 25°, and 81° and in-plane angles of 96°, 26°, and −72°. The in-plane projection angles 96° and 26° perfectly match those obtained through measuring the excitation polarization dependence of TPL, as demonstrated in column (d) of Figure 3.

Furthermore, as shown in Figure 4, the DOP of the TPL from AuNR2 is smaller than that from AuNR1, revealing that AuNR2 is really orientated out of plane. The defocused image of AuNR3 is nearly isotropic, and its TPL is independent of the excitation polarization. There are two possibilities for the appearance of this defocused pattern. One is that the long axis of the AuNR is almost perpendicular to the glass substrate. It is also possible that AuNR3 is an aggregation of several AuNRs.

These perfectly matched results reveal that from the defocused imaging analysis not only can the accurate 2D in-plane projection information be deduced, but the out-of-plane angle information can also be resolved directly, indicating that this technique is very informative. More importantly, it can be utilized to obtain live images and simultaneously track and monitor multiple dynamic events with a fast data acquisition rate. As large numbers of AuNRs can be monitored in parallel within a single frame, it is capable of achieving high throughput for sensing. Therefore, the orientation sensor based on defocused imaging of individual AuNRs is an ideal candidate for optical imaging and sensing various reaction processes in materials science and biological applications.

In the following, we investigate the influence of the excitation to examine the flexibility of this technique.

The intensities integrated over the whole defocused image and the wavelength range from 540 to 910 nm are plotted as a function of the incident polarization angle in Figure 5a and b for two randomly selected AuNRs. The insets show the defocused images of the individual AuNRs for different polarization angles. It can be clearly seen that although the intensity response of the defocused images is accordingly varied with the incident polarization, the pattern of the defocused images, however, remains unchanged regardless of the NR orientation, suggesting that the emission from the dipole oscillating along the long axis is always dominant. As we know, plasmon scattering in AuNRs is polarized along the long rod axis for the longitudinal mode and the perpendicular direction for the transverse mode. If their single-photon luminescence (SPL) behavior is similar to their scattering, the pattern of the defocused image of individual AuNRs would rotate 90° when the excitation polarization is changed from parallel to perpendicular to the long axis of the rod, as 532 nm is close to the transverse surface plasmon resonance. It seems the polarization characteristic of their emission is different from their scattering.

A very recently published paper reported that when AuNRs are excited by a wavelength of 514 nm (CW), both d−sp interband transitions and the transverse surface plasmon can be excited due to their spectral overlap. A fast interconversion between the created electron−hole pairs and the transverse surface plasmons that subsequently decays radiatively may lead to a loss of polarization (absorption and emission) for the short-wavelength peak in the AuNR luminescence spectra.[45] This means that the emission at the short-wavelength peak exists in all directions regardless the polarization direction of the excitation. However, the longitudinal plasmon luminescence is independent of the excitation only and always occurs along the long axis of the AuNR. In our case, although the 532 nm excitation is a little red-shifted and positioned at the red edge of the transverse surface plasmon resonance, we believe that the properties of the emission related with the transverse mode should be similar to that excited by 514 nm. Under this assumption, we can explain why the emission from individual AuNRs cannot be described by a single dipole in our experiments and their defocused image has to be fitted by a multidimensional dipole model. Furthermore, as the longitudinal plasmon luminescence always occurs along the long axis of the AuNR, the pattern of the defocused image always exhibits dominant emission from the long axis, as we have seen in Figure 5. On the other hand, 532 nm is closer to the longitudinal surface plasmon resonance than 514 nm. When the excitation polarization is parallel to the long axis of the AuNR, the excitation efficiency seems higher than when perpendicular. Therefore, there is obvious

excitation polarization dependence for the intensity integrated over the whole defocused images and the wavelength range from 540 to 910 nm. The intensity from parallel excitation is maximum. This analysis
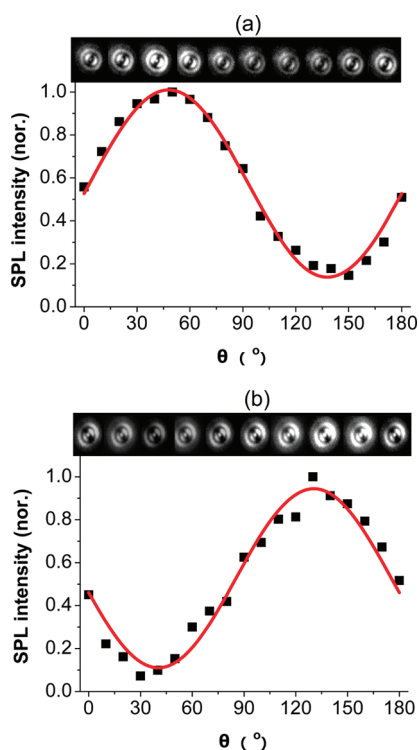
Figure 5. Excitation polarization dependence of SPL intensity integrated over the defocused image area and in a wavelength range 540−910 nm for two randomly selected AuNRs with different spatial orientations. The top insets are the corresponding measured defocused images. Obviously, the pattern of the defocused images remains the same, although the intensity varies with the excitation polarization. (a) $\beta = 41°$, $\Psi = 0°$; (b) $\beta = 131°$, $\Psi = 0°$.

can be supported by the measurement of DOP for AuNRs with different aspect ratios. As can be seen in Figure S5, the DOP decreases with aspect ratio, suggesting that the contribution from the longitudinal mode decreases. One thing we need to note is that our present experiment system cannot resolve the two emission peaks corresponding to the transverse and longitudinal surface plasmon resonances, respectively. The spectra show broad bandwidth for both SPL and TPL. We are trying to improve the sensitivity of the system and trying other excitation wavelengths to understand the detailed mechanism. However, the constant pattern of defocused images means that any polarization can validate the probe within a single frame, and it is not necessary to insert a half-wave plate into the incident circuit to optimize the polarization direction. Furthermore, unlike scattering, the PL from AuNRs is not critically dependent on the excitation wavelength, as the absorption band is relatively broad.[46] The pattern of the defocused image is thus expected to be insensitive to the excitation.
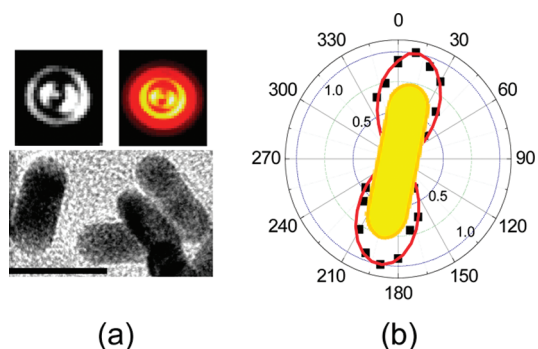
When the aspect ratio (R) of the AuNR is less than 5, the fundamental plasmon mode is dipolar in character, and the resonance peak of the mode shifts to the longer wavelength as the aspect ratio increases.[47] When $R > 5$, multipolar plasmon modes become dominant and multipolar oscillations would reduce the spatial confinement and produce a reduction of the field enhancement. As the defocused imaging method is based on the dipole approximation model, we controlled the aspect ratio of AuNR to be less than 5, in which the emission can be approximated to be from three perpendicularly positioned single dipoles. Figure 6a displays the
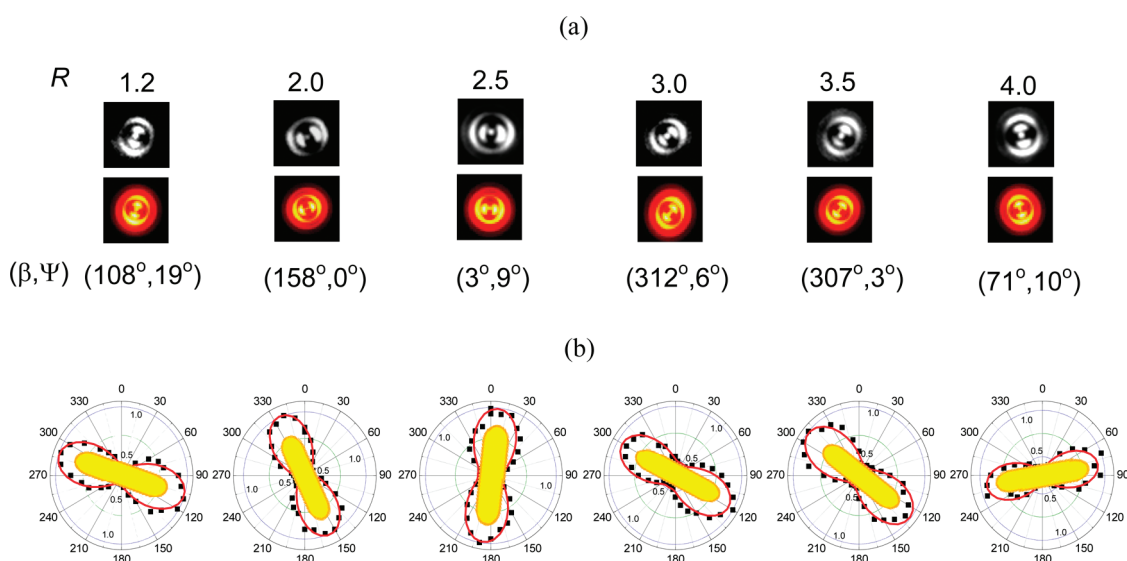
Figure 6. (a) Measured (top panel) and simulated (bottom panel) defocused images of single AuNRs with different aspect ratios, which are indicated at the top. (b) Polar plots of TPL intensities (black squares) *versus* the excitation polarization direction. The red curves are drawn according to the best-fitted $\cos^4(\theta - \beta)$ function. The orientations of the yellow rods are derived from the defocused images shown in (a).

defocused images from six individual AuNRs with aspect ratios of 1.2, 2.0, 2.5, 3.0, 3.5, and 4.0. The corresponding orientation information obtained from the defocused images and polarization characteristics of their TPL are shown in Figure 6b. Obviously, they are in good agreement.

There is normally a distribution of aspect ratios in the fabrication of AuNRs even when the growth parameters have been controlled very strictly.[48] As we know, the longitudinal SP resonance of the AuNRs is significantly dependent on their aspect ratios. For previously proposed orientation sensing techniques based on, for example, photothermal imaging, the excitations have to be tuned when the aspect ratio of the probes varies.[1,35] However, the SPL emission spectrum is quite broad, as shown in Figure S3b. The enhancement for the outgoing emitted light is expected to be valid for a large range of R. Furthermore, the brightness symmetry of the defocused image is very easily broken if there is a little difference between the emission from the two perpendicularly orientated dipoles. Therefore, in a large range of aspect ratios, the defocused image of AuNR exhibits anisotropy and possesses an orienta-

tion sensing function. The fabrication tolerance for this probe is thus very large. More importantly, we can apply the same light wavelength to excite the probe, which is highly desirable for optical imaging and sensing.

As smaller particles are more attractive in the language of minimizing potential interference from the probe itself, we exploit the size effect on the defocused images of AuNRs. We fabricated much smaller AuNRs according to the method proposed in ref 49. Figure 7a exhibits a representative TEM image. The diameter and length of the AuNRs was determined to be about 9 and 20 nm on average, which corresponds to an effective diameter of 12 nm for a sphere. A typical defocused image taken from this sample is demonstrated at the top of Figure 7a. Evidently, it exhibits a similar pattern to those from larger AuNRs shown in the above text. We also tracked the TPL intensity upon tuning the excitation polarization, as displayed in Figure 7b. It was found that the orientations obtained by these two techniques are consistent, revealing that defocused imaging can measure the spatial orientation of individual AuNRs as small as 10 nanometers.

Last, we discuss the influence of the defocusing distance, as it affects the defocused pattern seriously.[25] Figure 8 shows a series of seven defocused images for the same AuNR when the defocused distance was varied from 0 to 1.2 μm. The upper panel shows the experimental results, and the lower panel the simulated images. We can find a fair correspondence between them. Obviously, when the defocused distance is in the range 0.5−1.2 μm, the defocused patterns exhibit anisotropy and the in-plane orientation can be derived easily. Figure S6 displays more detailed simulated results, in which all the in-plane orientations of individual AuNRs can be deduced when the defocused distance is in the range 0.5−1.2 μm. However, only the brightness symmetry of the high-order diffraction ring and the bright spot near the center of the defocused image can provide accurate information on the out-of-plane angle, as we have discussed in Figure S4. In this case, the defocused distance has to be carefully adjusted to be around 0.95−1.05 μm.
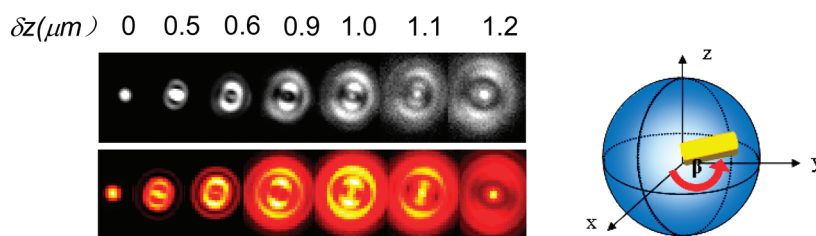

(a)

(b)

Figure 7. (a) Representative TEM image for the fabricated AuNRs with smaller sizes. The scale bar dimension is 20 nm. The top insets show the measured (in black and white) and simulated (in red and yellow) defocused images of a typical AuNR with the diameter and length as small as about 9 and 20 nm on average. β and Ψ are derived to be 10° and 14°, respectively. (b) Polar plot of the TPL intensity (black squares) *versus* the excitation polarization direction. The red curves are drawn according to the best-fitted $\cos^4(\theta-\beta)$ function. The orientation of the yellow rod is derived from the defocused image.

$\delta z (\mu m)$ 0   0.5   0.6   0.9   1.0   1.1   1.2

Figure 8. (a) Measured (top panel) and simulated (bottom panel) defocused images of the same AuNR with an aspect ratio of 2.5 at different defocusing distance δz, which is illustrated at the top. $\delta z = 0$ corresponds to the focal plane. The spatial orientation of the AuNR is schematically plotted at right.

CONCLUSIONS

To conclude, we have validated a novel nonphotobleaching and nonphotoblinking optical orientation sensor at the nanoscale by defocused imaging of individual AuNRs with a common wide-field microscope. By simultaneously measuring the polarization characteristic of TPL for a large number of individual AuNRs with aspect ratios of 1.2–4, we correlate their defocused images with their three-dimensional spatial orientations. Compared with previous reports, the orientation probes proposed in our paper are independent of the polarization and wavelength of the exciting source, the size can be as small as 10 nanometers, and the distribution of the aspect ratio was determined to have negligible effects on the sensing property. Furthermore, since deciphering the images can be finished off-line at a later time and many AuNRs can be monitored parallel within a single frame, video-rate acquisition of multiple AuNRs is possible and the probing is highly effective. These unique features make the orientation probes demonstrated in this paper outstanding candidates for optical imaging and sensing in materials science and biological applications.

METHODS

Preparation of Samples. AuNRs were prepared chemically in aqueous solutions by a seed-mediated method.[39] Briefly, a seed sphere solution with 3–5 nm Au nanocrystals was generated by adding ice-cold $NaBH_4$ to a solution of $HAuCl_4$ in the presence of cetyltrimethylammonium bromide (CTAB). This light brown seed solution was vigorously stirred for 30 min and then kept at room temperature before further used. To make a growth solution, 400 μL of 25 mM $HAuCl_4$ and 10 mL of 0.2 M CTAB were mixed with 10 mL of deionized water (18 MΩ), followed by the addition of 100 μL of 4.0 mM $AgNO_3$ solution. Then, 200 μL of 0.08 M ascorbic acid was added, and the solution gently stirred for 30s, which changed the color of the growth solution from orange to transparent. The growth of AuNRs was initiated by injecting 24 μL of the seed solution into the growth solution. After leaving for 24 h at room temperature, the AuNRs could be purified from the excess surfactant solution by centrifugation (13 000 rpm for 15 min). The aspect ratio of AuNRs can be controlled by tuning the concentration of $AgNO_3$ in the growth solution.

We utilized two methods to deposit AuNRs onto the glass coverslips. In the first method, we dropped the synthesized AuNRs onto a glass coverslip with another one on the top. Then the two coverslips were separated. The positively charged AuNRs are likely attached to the negatively charged coverslip tightly, and most of them are parallel to the substrate. In the second method, we dropped the mixture consisting of the synthesized AuNRs and 15% PVA solutions by a volume ratio of 1:1 between two coverslips. Then we separated the two coverslips very carefully. PVA can help the AuNRs to be unparallel to the substrates because of its high viscosity.

Defocused Imaging and TPL Polarization Dependence Measurement of Individual AuNRs. The details of our experimental setup to investigate the defocused image and TPL polarization dependence of individual AuNRs are similar to what was shown in our previous papers[40,41] and schematically plotted in Figure S1. In brief, the samples were excited by a diode-pumped solid-state laser (532 nm, 10 kW/cm^2, Coherent) that is directed through a Zeiss 100×/1.3NA oil immersion objective. A half-wave plate was inserted into the incident circuit to rotate the polarization of the excitation with respect to the laboratory reference system from 0° to 180° with 10° increments. In order to improve the signal-to-noise ratio, the size of the beam from the laser was reduced before it entered into the microscope. With a long pass filter to block the excitation light in the detection path, the PL from AuNRs was collected by the same objective and detected using an intensified charge-coupled device (CCD) (Carl Zeiss) camera, as shown in the Supporting Information (Figure S1). The defocused image was taken by moving the objective around 1 μm toward the sample after a clear diffraction-limited fluorescence image appeared. All the fluorescence images were recorded at room temperature. The exposure time for each image was set to be 200 ms in order to obtain enough signal-to-noise ratio. As the fluorescence emission intensity from individual AuNRs is comparable with that from CdSe/ZnS quantum dots (refer to the Supporting Information), the signal to background ratio is much higher for individual AuNRs because of the enhanced excitation intensity and the shrinkage of the excitation point at the sample. The effect can be clearly seen in Figure S1.

For TPL polarization dependence measurement, a 800 nm laser pulse (130 fs and 76 MHz, 10 nJ/mm^2) from a Ti:sapphire oscillator (Mira 900, Coherent) was used as the excitation source. The excitation polarization was controlled by a half-wave plate operating at 800 nm in the incident circuit. The SPL (TPL) spectrum of individual AuNRs in focus was measured by an Andor electron-multiplying CCD (EMCCD, DU970N-BV, and DU-897E) together with a 540–910 nm (370–720 nm) bandpass filter in the output circuit. The details for the measurement are described in the caption of Figure S1. We normally choose the target AuNR by first tracking its TPL intensity upon rotating the excitation polarization. After that, we change the excitation wavelength to 532 nm and record the defocused images. The optical circuit has to be adjusted very carefully to ensure that we are probing the same AuNR during these two processes.

Conflict of Interest: The authors declare no competing financial interest.

Supporting Information Available: Fluorescence imaging and spectrum analyzing system; the definition of the 3D orientation of the NR; TPL and SPL spectra for individual AuNRs; calculated defocused images for AuNRs with different spatial orientations; DOP as a function of aspect ratio; calculated defocused patterns for AuNRs with different in-plane orientations and different defocused distances. This material is available free of charge *via* the Internet at http://pubs.acs.org.

REFERENCES AND NOTES

1. Chang, W.-S.; Ha, J. W.; Slaughter, L. S.; Link, S. Plasmonic Nanorod Absorbers as Orientation Sensors. *Proc. Natl. Acad. Sci. U. S. A.* **2010**, *107*, 2781–2786.
2. Sönnichsen, C.; Alivisatos, A. P. Gold Nanorods as Novel Nonbleaching Plasmon-Based Orientation Sensors for Polarized Single-Particle Microscopy. *Nano Lett.* **2005**, *5*, 301–304.
3. Higgins, D. A.; Luther, B. J. Watching Molecules Reorient in Liquid Crystal Droplets with Multiphoton-Excited Fluorescence Microscopy. *J. Chem. Phys.* **2003**, *119*, 3935–3942.
4. Bartko, A. P.; Xu, K.; Dickson, R. M. Three-Dimensional Single Molecule Rotational Diffusion in Glassy State Polymer Films. *Phys. Rev. Lett.* **2002**, *89*, 026101.

5. Link, S.; Chang, W.-S.; Yethiraj, A.; Barbara, P. F. Orthogonal Orientations for Solvation of Polymer Molecules in Smectic Solvents. *Phys. Rev. Lett.* **2006**, *96*, 017801.

6. Hu, D. H.; Yu, J.; Wong, K.; Bagchi, B.; Rossky, P. J.; Barbara, P. F. Collapse of Stiff Conjugated Polymers with Chemical Defects into Ordered, Cylindrical Conformations. *Nature* **2000**, *405*, 1030–1033.

7. Forkey, J. N.; Quinlan, M. E.; Shaw, M. A.; Corrie, J. E. T.; Goldman, Y. E. Three-Dimensional Structural Dynamics of Myosin V by Single-Molecule Fluorescence Polarization. *Nature* **2003**, *422*, 399–404.

8. Gould, T. J.; Gunewardene, M. S.; Gudheti, M. V.; Verkhusha, V. V.; Yin, S.-R.; Gosse, J. A.; Hess, S. T. Nanoscale Imaging of Molecular Positions and Anisotropies. *Nat. Methods* **2008**, *5*, 1027–1030.

9. Wang, G.-F.; Sun, W.; Luo, Y.; Fang, N. Resolving Rotational Motions of Nano-objects in Engineered Environments and Live Cells with Gold Nanorods and Differential Interference Contrast Microscopy. *J. Am. Chem. Soc.* **2010**, *132*, 16417–16422.

10. Kukura, P.; Ewers, H.; Müller, C.; Renn, A.; Helenius, A.; Sandoghdar, V. High-Speed Nanoscopic Tracking of the Position and Orientation of a Single Virus. *Nat. Methods* **2009**, *6*, 923–927.

11. Frantsuzov, P.; Kuno, M.; Jankó, B.; Marcus, R. A. Universal Emission Intermittency in Quantum Dots, Nanorods and Nanowires. *Nat. Phys.* **2008**, *4*, 519–522.

12. Moerner, W. E.; Orrit, M. Illuminating Single Molecules in Condensed Matter. *Science* **1999**, *283*, 1670–1676.

13. Dahan, M.; Lévi, S.; Luccardini, C.; Rostaing, P.; Riveau, B.; Triller, A. Diffusion Dynamics of Glycine Receptors Revealed by Single-Quantum Dot Tracking. *Science* **2003**, *302*, 442–445.

14. Kirchner, C.; Liedl, T.; Kudera, S.; Pellegrino, T.; Javier, A. M.; Gaub, H. E.; Stölzle, S.; Fertig, N.; Parak, W. J. Cytotoxicity of Colloidal CdSe and CdSe/ZnS Nanoparticles. *Nano Lett.* **2005**, *5*), 331–338.

15. Sau, T. K.; Rogach, A. L.; Jäckel, F.; Klar, T. A.; Feldmann, J. Properties and Applications of Colloidal Nonspherical Noble Metal Nanoparticles. *Adv. Mater.* **2010**, *22*), 1805–1825.

16. Sperling, R. A.; Gil, P. R.; Zhang, F.; Zanella, M.; Parak, W. J. Biological Applications of Gold Nanoparticles. *Chem. Soc. Rev.* **2008**, *37*, 1896–1908.

17. Van Dijk, M. A.; Tchebotareva, A. L.; Orrit, M.; Lippitz, M.; Berciaud, S.; Lasne, D.; Cognet, L.; Lounis, B. Absorption and Scattering Microscopy of Single Metal Nanoparticles. *Phys. Chem. Chem. Phys.* **2006**, *8*, 3486–3495.

18. Nehl, C. L.; Hafner, J. H. Shape-Dependent Plasmon Resonances of Gold Nanoparticles. *J. Mater. Chem.* **2008**, *18*, 2415–2419.

19. Schubert, O.; Becker, J.; Carbone, L.; Khalavka, Y.; Provalska, T.; Zins, I.; Sönnichsen, C. Mapping the Polarization Pattern of Plasmon Modes Reveals Nanoparticle Symmetry. *Nano Lett.* **2008**, *8*, 2345–2350.

20. Zijlstra, P.; Chon, J. W. M.; Gu, M. Five-Dimensional Optical Recording Mediated by Surface Plasmons in Gold Nanorods. *Nature* **2009**, *459*, 410–413.

21. Van der Zande, B. M. I.; Koper, G. J. M.; Lekkerkerker, H. N. W. Alignment of Rod-Shaped Gold Particles by Electric Fields. *J. Phys. Chem. B* **1999**, *103*, 5754–5760.

22. Zijlstra, P.; Chon, J. W. M.; Gu, M. White Light Scattering Spectroscopy and Electron Microscopy of Laser Induced Melting in Single Gold Nanorods. *Phys. Chem. Chem. Phys.* **2009**, *11*, 5915–5921.

23. Dedecker, P.; Muls, B.; Deres, A.; Uji-i, H.; Hotta, J.; Sliwa, M.; Soumillion, J.-P.; Müllen, K.; Enderlein, J.; Hofkens, J. Defocused Wide-Field Imaging Unravels Structural and Temporal Heterogeneity in Complex Systems. *Adv. Mater.* **2009**, *21*, 1079–1090.

24. Schuster, R.; Barth, M.; Gruber, A.; Cichos, F. Defocused Wide Field Fluorescence Imaging of Single CdSe/ZnS Quantum Dots. *Chem. Phys. Lett.* **2005**, *413*, 280–283.

25. Xiao, L. H.; Qiao, Y. X.; He, Y.; Yeung, E. S. Three Dimensional Orientational Imaging of Nanoparticles with Darkfield Microscopy. *Anal. Chem.* **2010**, *82*, 5268–5274.

26. Uji-i, H.; Deres, A.; Muls, B.; Melnikov, S.; Enderlein, J.; Hofkens, J. Defocused Imaging in Wide-Field Fluorescence Microscopy. In *Fluorescence of Supermolecules, Polymers, and Nanosystems*; Springer: New York, 2008; Chapter 4.

27. Mooradian, A. Photoluminescence of Metals. *Phys. Rev. Lett.* **1969**, *22*, 185–187.

28. Zheng, J.; Zhang, C. W.; Dickson, R. M. Highly Fluorescent, Water-Soluble, Size-Tunable Gold Quantum Dots. *Phys. Rev. Lett.* **2004**, *93*, 077402.

29. Mohamed, M. B.; Volkov, V.; Link, S.; El-Sayed, M. A. The `Lightning' Gold Nanorods: Fluorescence Enhancement of Over a Million Compared to the Gold Metal. *Chem. Phys. Lett.* **2000**, *317*, 517–523.

30. Dulkeith, E.; Niedereichholz, T.; Klar, T.; Feldmann, J.; von Plessen, G.; Gittins, D.; Mayya, K.; Caruso, F. Plasmon Emission in Photoexcited Gold Nanoparticles. *Phys. Rev. B.* **2004**, *70*, 205424.

31. Bouhelier, A.; Bachelot, R.; Lerondel, G.; Kostcheev, S.; Royer, P.; Wiederrecht, G. P. Surface Plasmon Characteristics of Tunable Photoluminescence in Single Gold Nanorods. *Phys. Rev. Lett.* **2005**, *95*, 267405.

32. Boyd, G. T.; Yu, Z. H.; Shen, Y. R. Photoinduced Luminescence from the Noble Metals and Its Enhancement on Roughened Surfaces. *Phys. Rev. B: Condens. Matter* **1986**, *33*, 7923–7936.

33. Zheng, J.; Nicovich, P. R.; Dickson, R. M. Highly Fluorescent Noble-Metal Quantum Dots. *Rev. Phys. Chem.* **2007**, *58*, 409–431.

34. Yuan, C. T.; Chou, W. C.; Tang, J.; Lin, C. A.; Chang, W. H.; Shen, J. L.; Chun, D. S. Single Fluorescent Gold Nanoclusters. *Opt. Express* **2009**, *17*, 16111–16118.

35. Wang, H.; Huff, T. B.; Zweifel, D. A.; He, W.; Low, P. S.; Wei, A.; Cheng, J.-X. In Vitro and in Vivo Two-Photon Luminescence Imaging of Single Gold Nanorods. *Proc. Natl. Acad. Sci. U. S. A.* **2005**, *102*, 15752–15756.

36. Imura, K.; Okamoto, H. Properties of Photoluminescence from Single Gold Nanorods Induced by Near-Field Two-Photon Excitation. *J. Phys. Chem. C* **2009**, *113*, 11756–11759.

37. Imura, K.; Nagahara, T.; Okamoto, H. Near-Field Two-Photon-Induced Photoluminescence from Single Gold Nanorods and Imaging of Plasmon Modes. *J. Phys. Chem. B* **2005**, *109*, 13214–13220.

38. Wu, X.; Ming, T.; Wang, X.; Wang, P.; Wang, J.; Chen, J. High-Photoluminescence-Yield Gold Nanocubes: for Cell Imaging and Photothermal Therapy. *ACS Nano* **2010**, *4*, 113–120.

39. Sau, T. K.; Murphy, C. J. Seeded High Yield Synthesis of Short Au Nanorods in Aqueous Solution. *Langmuir* **2004**, *20*), 6414–6420.

40. Li, Q.; Chen, X.-J.; Xu, Y.; Lan, S.; Liu, H.-Y.; Dai, Q.-F.; Wu, L.-J. Photoluminescence Properties of the CdSe Quantum Dots Accompanied with Rotation of the Defocused Wide-Field Fluorescence Images. *J. Phys. Chem. C* **2010**, *114*, 13427–13432.

41. Chen, X.-J.; Xu, Y.; Lan, S.; Dai, Q.-F.; Lin, X.-S.; Guo, Q.; Wu, L.-J. Rotation of Defocused Wide-Field Fluorescence Images after Blinking in Single CdSe/ZnS Core-Shell Quantum Dots. *Phys. Rev. B* **2009**, *79*, 115312.

42. Böhmer, M.; Enderlein, J. Orientation Imaging of Single Molecules by Wide-Field Epifluorescence Microscopy. *J. Opt. Soc. Am. B.* **2003**, *20*, 554–559.

43. Ming, T.; Zhao, L.; Yang, Z.; Chen, H.; Sun, L.; Wang, J.; Yan, C. Strong Polarization Dependence of Plasmon-Enhanced Fluorescence on Single Gold Nanorods. *Nano Lett.* **2009**, *9*, 3896–3903.

44. Dedecker, P.; Muls, B.; Deres, A.; Uji-i, H.; Hotta, J.; Sliwa, M.; Soumillion, J.-P.; Müllen, K.; Enderlein, J.; Hofkens, J. Defocused Wide-Field Imaging Unravels Structural and Temporal Heterogeneity in Complex Systems. *Adv. Mater.* **2009**, *21*, 1079–1090.

45. Tcherniak, A.; Dominguez-Medina, S.; Chang, W.-S.; Swanglap, P.; Slaughter, L. S.; Landes, C. F.; Link, S. One-Photon Plasmon Luminescence and Its Application to Correlation Spectroscopy as a Probe for Rotational and

Translational Dynamics of Gold Nanorods. *J. Phys. Chem. C* **2011**, *115*, 15938–15949.

46. Eustis, S.; El-Sayed, M. A. Aspect Ratio Dependence of the Enhanced Fluorescence Intensity of Gold Nanorods: Experimental and Simulation Study. *J. Phys. Chem. B* **2005**, *109*, 16350–16356.

47. Slaughter, L. S.; Chang, W.-S.; Swanglap, P.; Tcherniak, A.; Khanal, B. P.; Zubarev, E. R.; Link, S. Single-Particle Spectroscopy of Gold Nanorods beyond the Quasi-Static Limit: Varying the Width at Constant Aspect Ratio. *J. Phys. Chem. C* **2010**, *114*, 4934–4938.

48. Chirea, M.; Cruz, A.; Pereira, C. M.; Silva, A. F. Size-Dependent Electrochemical Properties of Gold Nanorods. *J. Phys. Chem. C* **2009**, *113*, 13077–13087.

49. Xu, J.; Li, S. Y.; Weng, J.; Wang, X. F.; Zhou, Z. M.; Yang, K.; Liu, M.; Chen, X.; Cui, Q.; Cao, M. Y.; Zhang, Q. Q. Hydrothermal Syntheses of Gold Nanocrystals: From Icosahedral to Its Truncated Form. *Adv. Funct. Mater.* **2008**, *18*, 277–284.